



Selenium-containing D–A–D-type dopant-free hole transport materials for perovskite solar cells

Yajie Fu^{a,1}, Yapeng Sun^{b,1}, Hao Tang^a, Lingyun Wang^a, Huangzhong Yu^{b,**}, Derong Cao^{a,*}

^a State Key Laboratory of Luminescent Materials and Devices, School of Chemistry and Chemical Engineering, South China University of Technology, Guangzhou, 510641, China

^b School of Physics and Optoelectronics, South China University of Technology, Guangzhou, 510641, China

ARTICLE INFO

Keywords:

Perovskite solar cells
Dopant-free
Hole-transporting materials
Selenium
Chalcogen

ABSTRACT

A novel selenium-containing D–A–D-type dopant-free hole-transport material with fused dithienobenzosele-nadiazole acceptor unit (DTBS) was designed, synthesized and applied in a perovskite solar cell (PSC). In addition, two dopant-free hole-transport materials were prepared as references with similar structure but different chalcogen elements (O for DTBF and S for DTBT) being used. The impact of chalcogen atom variation in the dopant-free hole-transport materials on the properties is systematically investigated, such as the physico-chemical, electrochemical, morphological feature and photovoltaic properties in PSC. The PSC fabricated with DTBS shows the power conversion efficiency value of 15.09% due to its high fill factor, which is much higher than those with the references (13.31% for DTBF and 11.65% for DTBT). Moreover, the PSCs fabricated with DTBS without encapsulation are operational with 77.8% performance retention under air condition after 30 days, which is much better than those prepared with doped spiro-OMeTAD (43.6%). The great stability for the DTBS-based PSC may be owing to the excellent thin film morphology and hydrophobicity of DTBS. Our work demonstrates that the selenium-containing organic compounds can act as the dopant-free hole-transport materials in PSC with both high efficiency and long stability being achieved.

1. Introduction

Hybrid organic-inorganic perovskite materials have exhibited great application potential in perovskite solar cells (PSCs) because of their exceptional properties such as strong optical absorption in the visible region, long charge carrier diffusion lengths, solution processable deposition, and tunable bandgap energy [1–4]. PSCs have drawn much attention over the past few years due to their rapid development with the power conversion efficiency (PCE) being remarkably increased to 25.5% [5]. Generally, the PSCs mainly consist of a transparent conductive oxide front electrode, an electron-transporting material, a perovskite layer, a hole-transporting material (HTM), and a back electrode of a noble metal or carbon [6]. As a key part of perovskite solar cell, HTM is indispensable in accelerating hole extraction, suppressing charge recombination and protecting perovskite layer of devices from water [7–10]. So far, 2,2',7,7'-tetrakis-(*N,N*-di-*p*-methoxyphenyl-amine)-9,9'-spiro-bifluorene (spiro-OMeTAD) is the most

state-of-the-art organic HTM in PSCs due to its excellent thin film morphology and desirable hole extraction capacity [11]. However, the high-cost multistep synthesis and difficult purification for spiro-OMeTAD greatly hinder its large-scale application [12,13]. Moreover, spiro-OMeTAD suffers from low hole mobility and has to be doped with hydrophilic additives to increase the conductivity, which induce device instability and lead to complicated doping protocol [14]. In addition, the dopants also tend to react with molecules of oxidized spiro-OMeTAD to further accelerate device degradation process [15,16]. Therefore, it is necessary and challenging task to develop dopant-free HTMs as alternative materials for further improving PSCs.

So far, conjugated small molecules with well-defined molecular structures and tunable energy levels have been extensively explored to be the dopant-free HTMs for PSCs [17–20]. Several molecular design requirements can be concluded for developing highly efficient small molecule dopant-free HTMs. First, enhanced intermolecular interactions and π – π stacking are required to obtain dense film and improved hole

* Corresponding author.

** Corresponding author.

E-mail addresses: hzyu@scut.edu.cn (H. Yu), drcao@scut.edu.cn (D. Cao).

¹ Those authors contribute equally to this work.

mobility, which could be derived from planar rigid π -conjugated core structures, such as fused thiophene-based derivatives [21,22]. Second, donor–acceptor (D–A) type structures have been proven to be one of the major design strategies to prepare high performance dopant-free HTMs because their high charge carrier mobility due to strong dipolar intermolecular interactions, minimizing ohmic losses of the contact, good stability and high solubility [19,21,23]. Moreover, 4,4'-dimethoxytriphenylamine has been considered as the preferential terminal group in HTM designs owing to its easy oxidizability, strong electron-donating ability, efficient hole transport, and good film formation properties [23].

Based on above design principles, one potential candidate for acceptor units of HTMs could be fused dithieno[3',2':3,4; 2'',3'':5,6]benzo [1,2-c] [1,2,5]-chalcogenadiazole (DTBX, X = O, S, and Se). They have moderate electron withdrawing strength because of the fused two electron-rich thienyl rings, which might be beneficial to the electron blocking and hole transporting performance of the HTM layer [11]. Moreover, the DTBX-based molecules exhibit high charge carrier mobilities owing to the reduced conformational disorder arising from their four-ring-fused structure [24–27]. For the selenophene analogues, selenium atom in particular features larger size (atomic radius = 118 p.m.) than that of oxygen (atomic radius = 64 p.m.) or sulfur (atomic radius = 104 p.m.), which could obtain enhanced intermolecular interactions due to the increased chalcogen–chalcogen interactions arising from its larger atomic size [28]. Furthermore, selenium-containing molecules exhibit narrower bandgaps owing to the more polarizable nature of the selenium atoms, which lead to improved delocalization of electrons and thereby to a better conjugation [29,30]. Therefore, selenium-containing DTBX-based HTMs are expected to display improved charge extraction and charge mobility. However, the DTBX-based HTMs have been rarely reported for PSC applications, especially the selenium-containing DTBX-based HTMs in PSCs has not been reported yet. On the other hand, the atomic engineering of heterocyclic molecules is an effective approach for tuning the optical and electrochemical properties of the resulting organic optoelectronic materials. Some systematic investigations have been conducted on chalcogen-containing organic materials, revealing that the difference in the electron negativity and atomic size of chalcogen atoms has great impact on optical absorption, electronic property, backbone conformation, π – π stacking, morphological feature and photovoltaic properties in the organic optoelectronic devices [31–35]. Encouraged by these works, herein, we adopted acceptor units of dithieno[3',2':3,4; 2'',3'':5,6]benzo[1,2-c]furan, dithieno[3',2':3,4; 2'',3'':5,6]benzo[1,2-c][1,2,5]-thiadiazole and dithieno[3',2':3,4; 2'',3'':5,6]benzo[1,2-c][1,2,5]-selenadiazole as core in conjunction with methoxyl substituted triphenylamine (TPA) donors to design and synthesize three novel D–A–D HTMs (DTBF, DTBT, and DTBS) for dopant-free PSCs, as shown in Fig. 1. To the best of our knowledge, DTBS is the first selenium-containing dopant-free hole transport material in PSCs. We investigated the influences of the chalcogen atoms on the optical, thermal, electrochemical and photophysical properties of three dopant-free D–A–D HTMs. The PSCs based on these new dopant-free HTMs achieved good device performances where DTBS remarkably exhibited the highest photovoltaic performance among these three new HTMs with a PCE of 15.09%. Besides, the DTBS-based PSCs exhibited encouraging device stability with PCE maintaining 77.8% of their initial values after 30 days of aging in ambient air without encapsulation. The great stability for the PSCs with DTBS can be owing to the excellent thin

film morphology and hydrophobicity of DTBS.

2. Experimental

2.1. Materials and instruments

All chemicals were purchased from J&K and Sigma-Aldrich. Tetrahydrofuran (THF), toluene and 1,4-dioxane were purified over sodium under argon atmosphere. *N,N*-Dimethylformamide (DMF) was dried over molecular sieves. Other solvents were applied in analytical grade without further purification. The column chromatography separations were carried out on silica gel (300–400 mesh). ^1H and ^{13}C NMR spectra were measured on Bruker 400 MHz and 500 MHz instruments in CDCl_3 and $\text{DMSO}-d_6$, and tetramethylsilane (TMS) was used as internal standard. HRMS spectra were performed on an Agilent Technologies 1290 Infinity mass spectrophotometer.

2.2. Syntheses of HTMs

2.2.1. Synthesis of 2,7-dibromobenzo[1,2-b:6,5-b']dithiophene-4,5-dione (1)

BDTD (2.2 g, 10.0 mmol), NBS (3.74 g, 21.0 mmol), and DMF (100 mL) were mixed in a 250 mL round-bottom flask, heated to 65–70 °C, and stirred for 24 h. After the reaction was completed, the solution was poured into cold water, and a large amount of purple-black solid precipitated immediately. The resulting solid was filtered with a Buchner funnel, washed with hot water and dried. The sample was recrystallized from acetonitrile, collected by filtration, washed with acetonitrile, and dried under vacuum to obtain a dark purple solid 1 (3.47 g, 92%). ^1H NMR (400 MHz, CDCl_3) δ 7.46 (s, 2H). The spectroscopic description is in accordance with the published data [36].

2.2.2. Synthesis of 5,8-dibromodithieno[3',2':3,4; 2'',3'':5,6]benzo[1,2-c]furan (2)

Compound 1 (1.05 g, 3.0 mmol), hydroxylamine hydrochloride (0.52 g, 7.5 mmol), and ethanol (60 mL) were mixed in a 150 mL glass pressure vessel equipped with Teflon cap, stirred at 85 °C for 24 h and 140 °C for 48 h. After cooled to room temperature, the solvent was removed by rotary evaporation, and the resulting solid was washed with water. The solid was then purified by column chromatography with petroleum ether/dichloromethane ($v/v = 7/3$) as the eluent to give compound 2 (0.72 g, 56%) as yellow solid. ^1H NMR (400 MHz, CDCl_3) δ 7.92 (s, 2H). The spectroscopic description is in accordance with the published data [36].

2.2.3. Synthesis of 4,4'-(dithieno[3',2':3,4; 2'',3'':5,6]benzo[1,2-c][1,2,5]oxadiazole-5,8-diyl)bis(*N,N*-bis(4-methoxyphenyl)aniline) (DTBF)

A mixture of compound 2 (0.39 g, 1.0 mmol), compound 3 (0.95 g, 2.2 mmol), K_2CO_3 aqueous solution (2 M, 2 mL), $\text{Pd}(\text{PPh}_3)_4$ (116 mg, 0.1 mmol) and anhydrous THF (50 mL) was heated to reflux and stirred for 24 h under N_2 atmosphere. After cooled to room temperature, the mixture was added with water to quench the reaction and was extracted with CH_2Cl_2 for three times. The combined organic phase was washed with brine and dried over anhydrous MgSO_4 . After the organic solvent was removed under reduced pressure, the coarse product was purified by silica gel column chromatography with petroleum ether/ethyl



Fig. 1. Chemical structure of the HTMs.

acetate (v/v = 6/1) as the eluent. The product DTBF (0.65 g, 77%) was obtained as an orange solid. ^1H NMR (400 MHz, CDCl_3) δ 7.90–7.83 (m, 2H), 7.51–7.42 (m, 4H), 7.14–7.07 (m, 8H), 6.93 (d, J = 8.5 Hz, 4H), 6.91–6.83 (m, 8H), 3.81 (s, 12H). ^{13}C NMR (101 MHz, CDCl_3) δ 156.42, 149.38, 145.73, 145.40, 140.16, 134.82, 127.12, 126.81, 124.44, 122.87, 119.73, 117.35, 114.89, 55.56, 55.48. ESI-HRMS (m/z): $[\text{M}+\text{H}]^+$ calcd for $\text{C}_{50}\text{H}_{38}\text{N}_4\text{O}_5\text{S}_2$: 838.2284, found: 838.2291.

2.2.4. Synthesis of dithieno[3',2':3,4; 2'',3'':5,6]benzo[1,2-c][1,2,5]thiadiazole (4)

A mixture of BDTDA (2.0 g, 9.08 mmol), triethylamine (3.2 g, 31.8 mmol) and chloroform (40 mL) was stirred at 0 °C with the thionyl chloride (1.6 g, 13.6 mmol) being added dropwise. The reaction mixture was stirred for 1 h at room temperature and heated to reflux for 5 h. After the reaction was quenched with cold water, the mixture stirred for 30 min. The organic phase was collected and washed with water. After evaporation of the solvent, the residue was purified by column chromatography on silica gel eluting with petroleum ether/dichloromethane (v/v = 7/3) to give compound 4 (1.65 g, 73%) as a yellow powder. ^1H NMR (400 MHz, CDCl_3) δ 8.03 (d, J = 5.3 Hz, 2H), 7.54 (d, J = 5.2 Hz, 2H). The spectroscopic description is in accordance with the published data [35].

2.2.5. Synthesis of 5,8-dibromodithieno[3',2':3,4; 2'',3'':5,6]benzo[1,2-c][1,2,5]thiadiazole (5)

Compound 4 (1.07 g, 4.31 mmol), chloroform (60 mL) and bromine (1.51 g, 9.48 mmol) were added to a 250 mL round bottom flask. The mixture was heated to 70 °C, and stirred for 12 h. After the reaction mixture was cooled to room temperature, the resulting solid was filtered, washed with chloroform, and dried. A yellow solid compound 5 (1.64 g, 94%) was obtained. ^1H NMR (400 MHz, CDCl_3) δ 8.05 (s, 2H). The spectroscopic description is in accordance with the published data [35].

2.2.6. Synthesis of 4,4'-(dithieno[3',2':3,4; 2'',3'':5,6]benzo[1,2-c][1,2,5]thiadiazole-5,8-diyl)bis(*N,N*-bis(4-methoxyphenyl)aniline) (DTBT)

A mixture of compound 5 (0.41 g, 1.0 mmol), compound 3 (0.95 g, 2.2 mmol), K_2CO_3 aqueous solution (2 M, 2 mL), $\text{Pd}(\text{PPh}_3)_4$ (116 mg, 0.1 mmol) and anhydrous THF (50 mL) was heated to reflux and stirred for 24 h under N_2 atmosphere. After the sample was cooled to room temperature, water was added to quench the reaction. The mixture was extracted with CH_2Cl_2 for three times. The combined organic phase was washed with brine and dried over anhydrous MgSO_4 . The organic solvent was removed under reduced pressure, and the coarse product was purified by silica gel column chromatography with petroleum ether/ethyl acetate (v/v = 6/1) as the eluent. The DTBT (0.64 g, 76%) was obtained as an orange solid. ^1H NMR (400 MHz, CDCl_3) δ 8.05–7.91 (m, 2H), 7.57–7.46 (m, 4H), 7.19–7.09 (m, 8H), 7.01–6.93 (m, 4H), 6.92–6.81 (m, 8H), 3.84 (s, 12H). ^{13}C NMR (101 MHz, CDCl_3) δ 156.31, 150.44, 149.05, 144.21, 140.32, 133.55, 129.47, 127.03, 126.81, 125.13, 119.93, 117.55, 114.86, 55.53, 55.50. ESI-HRMS (m/z): $[\text{M}+\text{H}]^+$ calcd for $\text{C}_{50}\text{H}_{38}\text{N}_4\text{O}_4\text{S}_3$: 854.2055, found: 854.2050.

2.2.7. Synthesis of dithieno[3',2':3,4; 2'',3'':5,6]benzo[1,2-c][1,2,5]selenadiazole (6)

The compound BDTDA (2.0 g, 9.08 mmol) was dissolved in ethanol (50 mL), and heated to reflux for 2 h with the addition of a hot solution of selenium dioxide (1.1 g, 10.0 mmol). After cooling to room temperature, the resulting solid was filtered, washed with ethanol, and dried. The compound 6 (2.04 g, 76%) was obtained as a yellow solid. ^1H NMR (500 MHz, CDCl_3) δ 8.01 (d, J = 5.3 Hz, 2H), 7.48 (d, J = 5.2 Hz, 2H). The spectroscopic description is in accordance with the published data [35].

2.2.8. Synthesis of 5,8-dibromodithieno[3',2':3,4; 2'',3'':5,6]benzo[1,2-c][1,2,5]selenadiazole (7)

Compound 6 (1.27 g, 4.31 mmol), chloroform (60 mL) and bromine (1.51 g, 9.48 mmol) were mixed, heated to 70 °C, and stirred for 12 h. The reaction mixture was cooled to room temperature, and the resulting solid was filtered, washed with chloroform, and dried. A pale brown solid compound 7 (1.78 g, 91%) was obtained. Because of the low solubility of compound 7 in the conventional deuterated solvents, we were unable to get the NMR data.

2.2.9. Synthesis of 4,4'-(dithieno[3',2':3,4; 2'',3'':5,6]benzo[1,2-c][1,2,5]selenadiazole-5,8-diyl)bis(*N,N*-bis(4-methoxyphenyl)aniline) (DTBS)

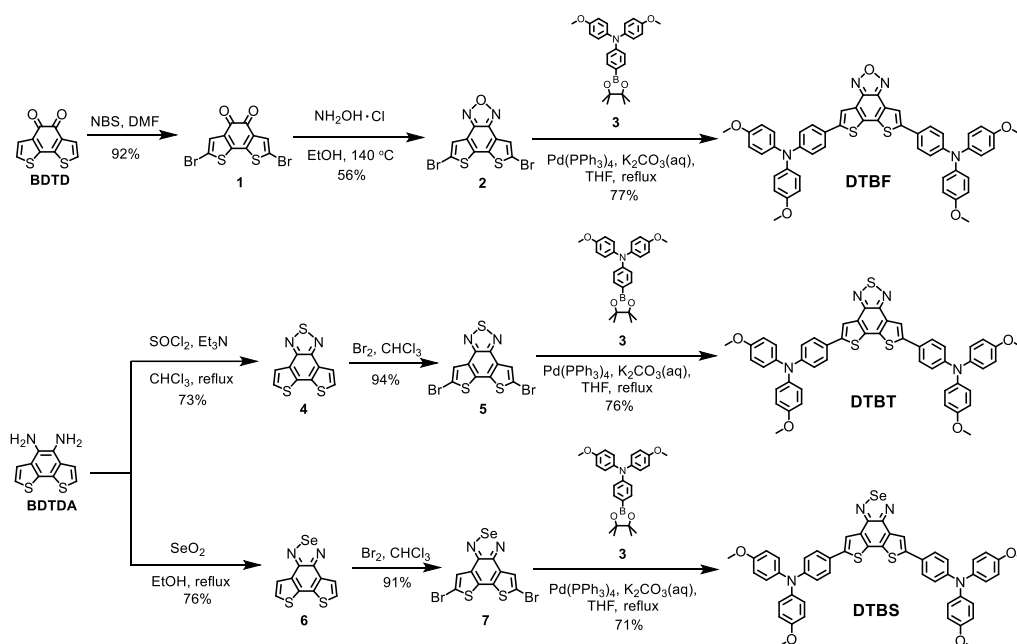
A mixture of compound 7 (0.45 g, 1.0 mmol), compound 3 (0.95 g, 2.2 mmol), K_2CO_3 aqueous solution (2 M, 2 mL), $\text{Pd}(\text{PPh}_3)_4$ (116 mg, 0.1 mmol) and anhydrous THF (50 mL) was heated to reflux and stirred for 24 h under N_2 atmosphere. After the cooling of mixture to room temperature, water was added to quench the reaction. The mixture was extracted with CH_2Cl_2 for three times. The combined organic phase was washed with brine and dried over anhydrous MgSO_4 . The organic solvent was removed under reduced pressure, and the coarse product was purified by silica gel column chromatography with petroleum ether/ethyl acetate (v/v = 5/1) as the eluent. The DTBS (0.64 g, 71%) was obtained as red solid. ^1H NMR (400 MHz, CDCl_3) δ 8.00–7.92 (m, 2H), 7.50 (d, J = 8.3 Hz, 4H), 7.18–7.08 (m, 8H), 6.99–6.93 (m, 4H), 6.92–6.86 (m, 8H), 3.84 (s, 12H). ^{13}C NMR (101 MHz, CDCl_3) δ 156.28, 155.86, 148.96, 143.78, 140.34, 133.78, 131.42, 127.01, 126.70, 125.19, 119.96, 118.39, 114.85, 55.53, 55.50. ESI-HRMS (m/z): $[\text{M}+\text{H}]^+$ calcd for $\text{C}_{50}\text{H}_{38}\text{N}_4\text{O}_4\text{S}_2\text{Se}$: 902.1500, found: 902.1494.

3. Result and discussion

The synthetic routes of DTBF, DTBT, and DTBS are illustrated in Scheme 1, and the characterization data are available in the experiment part. The compounds BDTD, BDTDA, 2, 3, 5, and 7 were synthesized by following the literatures [35–37]. The para-methoxy triphenylamine was then introduced by the Suzuki coupling reactions, resulting in three targeted HTMs, DTBF, DTBT, and DTBS in yields of 77%, 76%, and 71%, respectively.

The UV–vis absorption and photoluminescence spectra of DTBF, DTBT, and DTBS in CH_2Cl_2 solution were determined (Fig. 2a and Table 1). The absorption spectra of HTMs were characterized by two strong absorption bands from 300 to 600 nm where the peak at short wavelength can be ascribed to the local π – π^* electron transitions of core macrocyclic receptor conjugation system and the other absorption band (peaked at 480, 479 and 504 nm) can be ascribed to the intramolecular charge transitions (ICT) from the electron rich triphenylamine groups to the electron deficient core unit. Comparing with DTBF and DTBT, the bathochromic shift of DTBS originates from the better extended π -conjugation and stronger ICT interaction. In addition, the absorption spectra of three new HTMs in film states are shown in Fig. S10. The emission peaks of DTBF, DTBT, and DTBS were at 634, 643, and 687 nm, respectively. The optical energy band gap (E_g) can be determined according to the intersection of the normalized absorption and emission spectra, which are shown in Table 1.

The electrochemical properties of the three HTMs were investigated by performing cyclic voltammetry (CV) measurements (Fig. 2b), and the corresponding data are summarized in Table 1. The results indicate that the highest occupied molecular orbital (HOMO) values of DTBF, DTBT, and DTBS are –5.03, –5.00, and –5.05 eV, respectively, which could match well with the valence band (VB) of the perovskite (–5.4 eV) and result in adequate driving force for hole injection. In addition, the lowest unoccupied molecular orbital (LUMO) levels of DTBF, DTBT, and DTBS were –2.76, –2.72, and –2.89 eV, respectively. All the three HTMs have higher LUMO levels than the conduction band (CB) of the perovskite (–3.9 eV), suggesting that the transfer of the photogenerated electrons from the perovskite to the HTM layer and the recombination of a hole



Scheme 1. Synthetic routes of the HTMs.

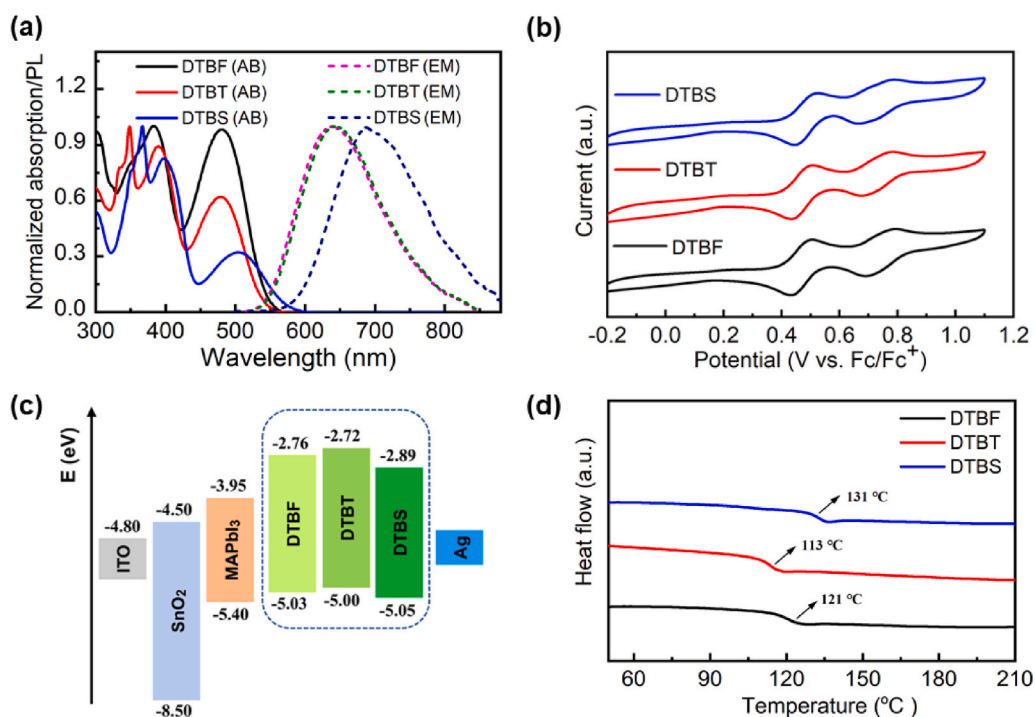


Fig. 2. a) Normalized absorption and emission curves for HTMs in CH_2Cl_2 solution. b) Cyclic voltammetry of DTBF, DTBT, and DTBS in CH_2Cl_2 solution. c) Energy level diagram. d) Differential scanning calorimetry curves of the three HTMs.

and an electron are effectively inhibited.

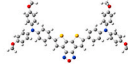
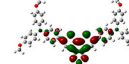
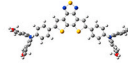
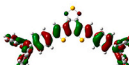
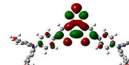
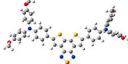
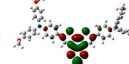
To further evaluate the properties of the three HTMs, the thermal stability of films was studied by differential scanning calorimetry (DSC) measurements, performed with two heating and cooling circles, and the result analysis is based on the second heating process. The result shows that the glass transition temperature (T_g) of DTBF, DTBT, and DTBS are 121, 113, and 131 °C, indicating their good morphological stability, which is beneficial to corresponding device stability (Fig. 2d) [8]. Besides, no obvious melting peak appeared on DSC scan curves indicates that all three HTMs are amorphous.

In order to better understand the geometrical configuration and electron distribution of the three new HTMs, quantum chemical calculations based on the density functional theory (DFT) were performed by employing the Gaussian 09 program at the B3LYP/6-31G (d) level. The optimized molecular structures and electron distributions in HOMO and LUMO energy levels of DTBF, DTBT, and DTBS are obtained and depicted in Table 2. The HOMO energy levels of the three HTMs are largely distributed on the whole molecular skeleton, while the LUMO energy levels are mainly localized on the central core unit. The well overlapped HOMO and LUMO levels orbits on the core unit suggest that

Table 1
Optical Properties, and Electrical Properties of three HTMs.

HTMs	λ_{abs}^a (nm)	λ_{em}^b (nm)	λ_{int}^c (nm)	Tg (°C)	E_g^d (eV)	HOMO ^e (eV)	LUMO ^f (eV)
DTBF	480	634	547	121	2.27	-5.03	-2.76
DTBT	479	643	543	113	2.28	-5.00	-2.72
DTBS	504	687	575	131	2.16	-5.05	-2.89

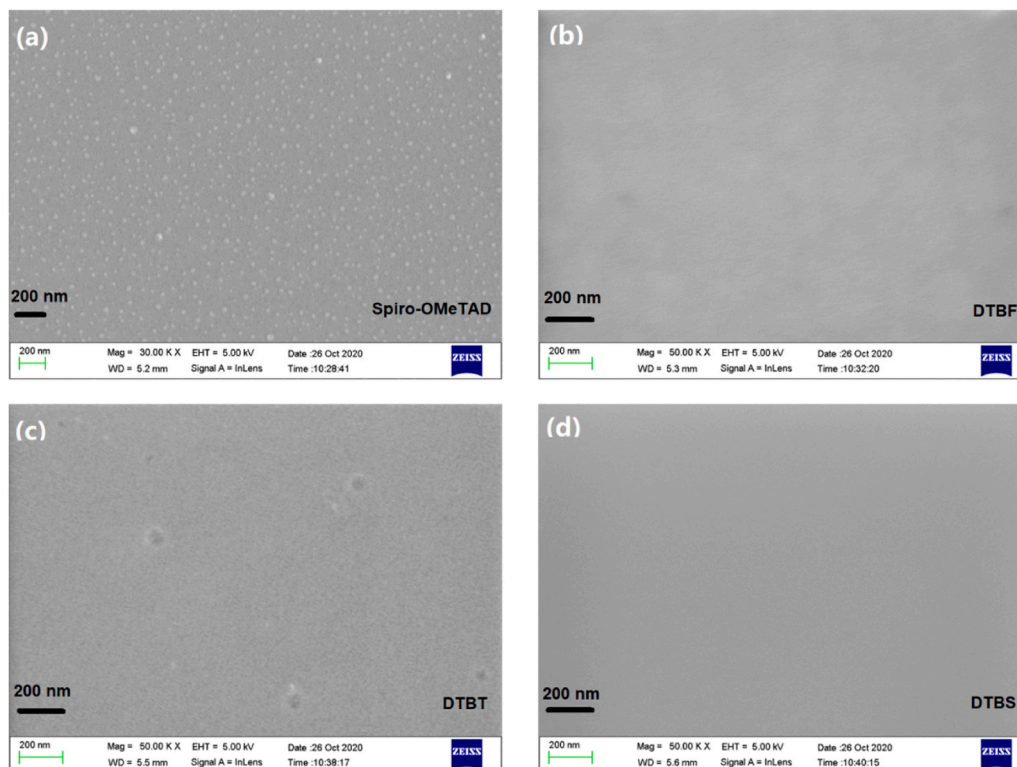
^a Absorption peak values of three HTMs in CH₂Cl₂ solution.^b Emission peak values of three HTMs in CH₂Cl₂ solution.^c The point of intersection of normalized absorption and emission spectra of three HTMs in CH₂Cl₂ solution.^d Calculated by the equation of $E_g = 1240/\lambda_{\text{int}}$.^e Calculated from the onset oxidation potentials of CV measurements.^f Calculated by the equation of $E_{\text{LUMO}} = E_{\text{HOMO}} + E_g$.**Table 2**
Results of DFT calculation (optimized structures, electron distributions in HOMO and LUMO energy levels) of the three HTMs.

HTMs	Top view	Side view	HOMO	LUMO
DTBF			 -4.62 eV	 -2.01 eV
DTBT			 -4.55 eV	 -2.01 eV
DTBS			 -4.51 eV	 -2.08 eV

the electron-withdrawing DTBX core unit can promote the charge transfer from the donor to the acceptor, which contributes to exciton generation and hole transfer [38,39]. In addition, the calculated HOMO energy levels of DTBF, DTBT, and DTBS are -4.62, -4.55, and -4.51 eV, while the LUMO energy levels are -2.01, -2.01 and -2.08 eV, respectively.

In general, a smooth and dense surface coverage of the perovskite layer by HTM films is highly beneficial for suppressing interfacial charge recombination to obtain efficient charge collection and thus a high PCE of devices [40]. The morphological characteristics of different HTMs on MAPbI₃ films were investigated by scanning electron microscopy (SEM) measurement and exhibited in Fig. 3a-d. The HTM DTBS presented uniform, smooth and pin-free thin film covering the underlying perovskite layer, indicating that DTBS molecule formed excellent films, which could prevent the harmful direct contact between the perovskite and the Ag back electrode, and thus facilitate the charge transport in PSCs.

To estimate the charge transport properties in the perovskite layers with the three HTMs, hole-injection only devices were fabricated with the structure of ITO/PTAA/MAPbI₃/HTL/Ag, where HTL was either DTBF, DTBT, DTBS or doped spiro-OMeTAD. According to the space charge limited current (SCLC) method, the devices were measured under dark conditions to obtain corresponding log *J*-*V* curves (Fig. 4a). As shown in Fig. 4a, the plot can be divided into three clearly defined regions based on the slope of the log *J*-*V* curves, that is, the ohmic region (the slope of the curve is close to 1), the SCLC region (the slope of the curve is close to 2) and the electroconvection region (the middle part of the curve, at which the slope of the curve is more than 3) [41,42]. The hole mobility can be calculated based on the data in the SCLC region. Hole mobility values of 3.11×10^{-5} , 2.35×10^{-5} , 5.29×10^{-5} , and 6.89×10^{-5} cm² V⁻¹ s⁻¹ were calculated for DTBF, DTBT, DTBS, and doped spiro-OMeTAD, respectively. Besides, the hole mobility of doped spiro-OMeTAD was also measured to be 1.92×10^{-5} cm² V⁻¹ s⁻¹ (Fig. S11), which is lower than those of three dopant-free HTMs. Obviously, though slightly lower than the value of doped spiro-OMeTAD, DTBS achieved the highest hole mobility among the three new HTMs,

**Fig. 3.** Top-view SEM images of the surface morphology of a) spiro-OMeTAD, b) DTBF, c) DTBT, and d) DTBS.

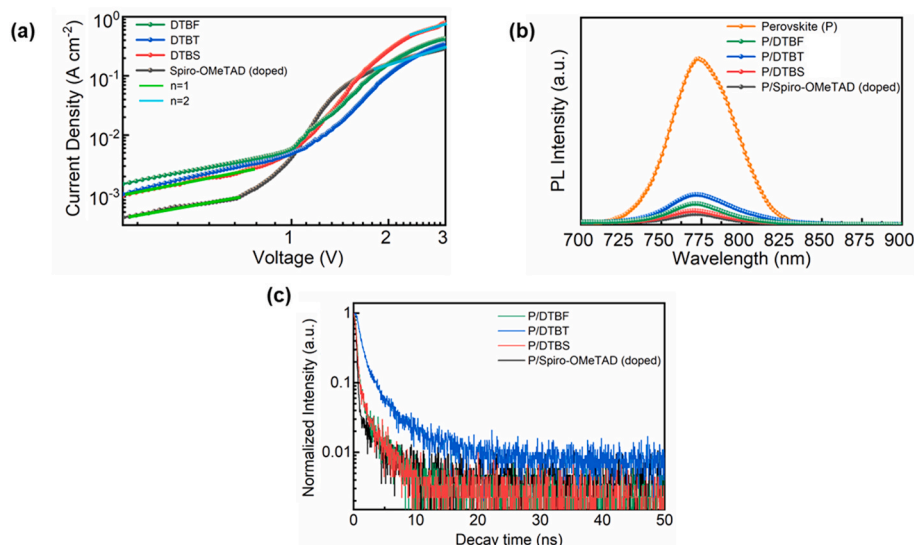


Fig. 4. a) Hole-mobility measurements for DTBF, DTBT, and DTBS. b) Steady-state PL spectra of the MAPbI₃ perovskite films with or without different HTMs. c) Time-resolved PL spectra of the MAPbI₃ perovskite films with different HTMs.

which suggests a faster hole transportation after the interfacial extraction. The higher mobility for DTBS could be ascribed mainly to its molecular framework and perfect film morphology. In addition, the dark current-voltage curves of the three new HTMs and doped spiro-OMeTAD were determined with a reported method [43]. As shown in Fig. S12, the result demonstrates that DTBS-based device exhibited smallest series resistance among three new HTMs.

To evaluate the hole transfer property at the interface between the perovskite and HTL, we investigated the steady-state photoluminescence (PL) and time-resolved photoluminescence (TRPL) spectra of the perovskite/DTBF, perovskite/DTBT, perovskite/DTBS, and perovskite/spiro-OMeTAD. As shown in Fig. 4b, the perovskite layer exhibits a strong PL peak at 775 nm. The bare perovskite exhibits a strong fluorescence peak and the PL intensity was significantly weakened for the device with different HTMs. This result indicates that holes can be efficiently transferred from the perovskite films to the HTMs [44]. Besides, for the reduction of PL, DTBS is most obvious among the three new HTMs, suggesting the most efficient charge injection at the

DTBS/perovskite interface. The TRPL spectra are illustrated in Fig. 4c and the relevant data are summarized in Table S1. The results show that the perovskite with DTBS exhibits a shorter PL lifetime ($\tau_{\text{ave}} = 1.79$ ns) than DTBF ($\tau_{\text{ave}} = 1.81$ ns) and DTBT ($\tau_{\text{ave}} = 3.40$ ns), which is close to doped spiro-OMeTAD ($\tau_{\text{ave}} = 1.21$ ns). Obviously, the results are consistent with the steady-state PL study, indicating that the hole transfer from the perovskite to the DTBS are more efficient than those of DTBF and DTBT.

Fig. 5b exhibits the J - V curves of DTBF, DTBT, DTBS, and doped spiro-OMeTAD based PSCs with MAPbI₃ used as the light absorber (Fig. 5a), and these key parameters are shown in Table 3. The dopant-free DTBF-based device achieved a PCE of 13.31% with an open-circuit voltage (V_{OC}) of 0.95 V, a short-circuit current (J_{SC}) of 22.48 mA cm⁻², and a fill factor (FF) of 62.3%. The dopant-free DTBT-based device showed a V_{OC} of 0.93 V, a J_{SC} of 22.20 mA cm⁻² and an FF of 56.1%, yielding a PCE of 11.65%. The dopant-free DTBS-based device obtained a V_{OC} of 0.96 V, a J_{SC} of 22.78 mA cm⁻² and an FF of 69.1%, yielding a PCE of 15.09%. These parameters of the PSCs based on DTBS

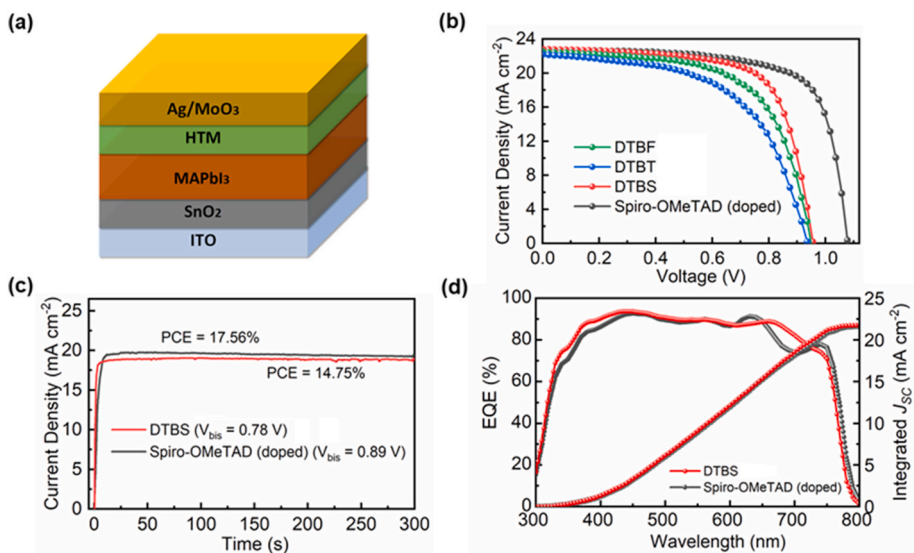


Fig. 5. a) Device architecture of PSCs. b) Reverse scan J - V curves for the best-performing devices using DTBF, DTBT, DTBS, and doped spiro-OMeTAD as HTMs. c) Stabilized power output at the maximum power point voltage of the devices based on DTBS (0.78 V) and spiro-OMeTAD (0.89 V). d) The IPCE curves of PSCs based on DTBS and spiro-OMeTAD.

Table 3

Photovoltaic parameters of the PSCs using dopant-free HTMs DTBF, DTBT, DTBS, and doped spiro-OMeTAD^{a,b}.

HTMs	J_{SC} (mA cm ⁻²)	V_{OC} (V)	FF (%)	PCE_{max} (%)	$PCE_{ave. \pm SD}$ (%) ^c
DTBF	22.48	0.95	62.3	13.31	11.91 ± 0.94
DTBT	22.20	0.93	56.1	11.65	10.26 ± 0.94
DTBS	22.78	0.96	69.1	15.09	13.66 ± 0.88
Doped spiro-OMeTAD	22.61	1.08	72.2	17.62	16.41 ± 0.76

^a Performances of devices measured using a 0.15 cm² working area.

^b Values refer to the cell with the optimal PCE.

^c Calculated on the basis of 15 measurements.

are slight lower than that for the doped spiro-OMeTAD-based device (a V_{OC} of 1.08 V, a J_{SC} of 22.61 mA cm⁻², an FF of 72.2%, and an overall PCE of 17.62%). The J_{SC} , V_{OC} , and FF values of the DTBS-based device are higher than those of DTBF- and DTBT-based devices. In addition, the undoped spiro-OMeTAD-based devices were also prepared to compare with the devices with three dopant-free HTMs. As shown in Fig. S14 and Table S2, the undoped spiro-OMeTAD-based devices exhibited a PCE of 7.36%, which is much lower than those of the devices based on three new dopant-free HTMs. The enhanced J_{SC} for the DTBS-based PSCs is in good consistent with the integral J_{SC} from the IPCE spectra with deviations less than 5% (Fig. 5d). The higher V_{OC} and FF value in PSCs can be ascribed to the relatively lower-lying HOMO level and the higher hole-mobility of DTBS, respectively. The statistical PCE distribution histograms of 15 PSC devices based on three new dopant-free HTMs and doped spiro-OMeTAD are displayed in Fig. 6 and the corresponding statistical parameters are listed in Table 3. The small standard deviation (SD) values demonstrate a good PCE reproducibility for those new HTMs-based PSC devices. Besides, the hysteresis phenomena of the devices containing DTBS and spiro-OMeTAD were investigated under reverse and forward scan directions (Fig. S15 and Table S3). The hysteresis index (HI) values of the PSCs with DTBS and spiro-OMeTAD are 8.3% and 6.0%, respectively. The results demonstrated the small hysteresis effects of the undoped DTBS-based devices, which may indicate

the few trap states in the devices. To assess the device stability of the PSCs, the stabilized power output over time was recorded at the maximum power point bias. As shown in Fig. 5c, both DTBS and spiro-OMeTAD based PSCs exhibit stabilized efficiencies (after 300 s) with a steady-state PCE of 14.75% and 17.56%, respectively.

The stability test of PSCs with DTBS and doped spiro-OMeTAD as a HTM without encapsulation was tested under air conditions (25 °C and 50% humidity) (Fig. 7). The DTBS-based PSC was operational with 77.8% performance retention after 30 days. By contrast, the PSC device based on doped spiro-OMeTAD maintained only 43.6% of its initial PCE under the same working conditions. The greater stability of DTBS-based device can be partially owing to its smooth HTM film acting as an effective moisture barrier. Moreover, the water contact angle (WCA) measurements of DTBS and spiro-OMeTAD were carried out on the HTM-coated film in the HTM/perovskite/SnO₂/ITO structure and the corresponding images were determined (Fig. 7). Compared to spiro-

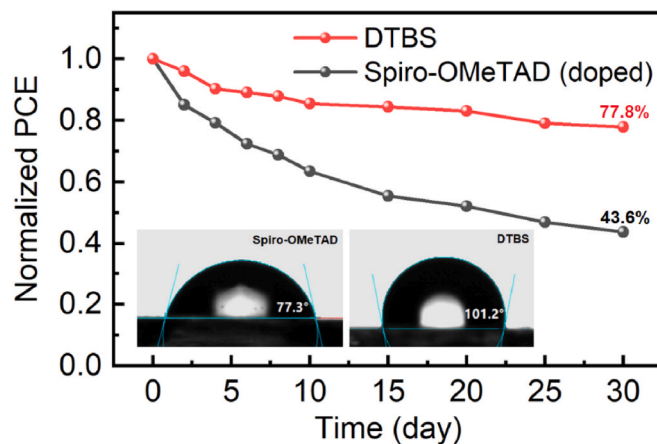


Fig. 7. Long-term stability of the PSC based on doped spiro-OMeTAD and DTBS under the relative humidity of 50% at 25 °C. The inset shows water contact angles on spin-coated films of spiro-OMeTAD and DTBS.

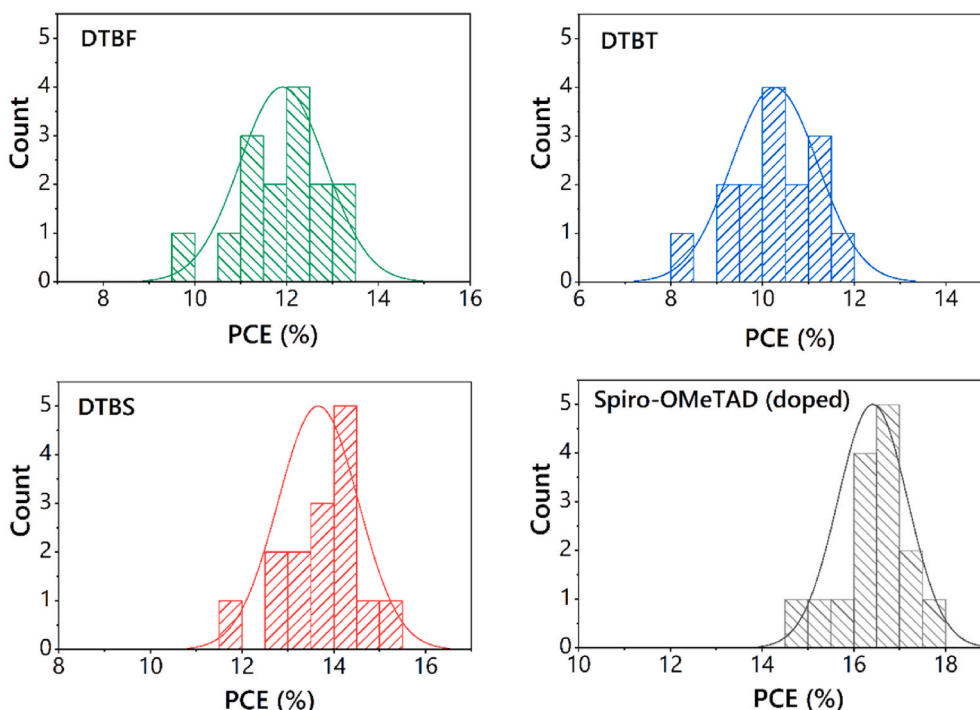


Fig. 6. Histogram of PCEs measured at 15 devices employing DTBF, DTBT, DTBS, and doped spiro-OMeTAD as HTMs, respectively.

OMeTAD (77.3°), significantly larger contact angles in DTBS (101.2°) coated films tend to show better protection from moisture for the underlying perovskite layer, and appear to be accord with the better time stability of the PSCs.

4. Conclusion

In summary, we have successfully designed and synthesized three D–A–D-type dopant-free HTMs (DTBF, DTBT, and DTBS) with triphenylamine as a donor and fused dithieno[3',2':3,4; 2'',3'':5,6]benzo[1,2-c][1,2,5]-chalcogenadiazole (DTBX, X = O, S, and Se) unit as an acceptor for applications in PSCs. The influence of the chalcogen atom of the three HTMs on optical and electronic properties and their solar cell performance was systematically investigated. The PSCs based on selenium-containing DTBS affords a PCE value of 15.09% without any dopants, comparable to that of the solar cell fabricated with doped spiro-OMeTAD (17.62%). Moreover, DTBS-based PSCs exhibit much better long-term stability than spiro-OMeTAD due to the superior hydrophobicity of DTBS. Our results not only indicate that the substituted chalcogen atoms in the DTBX unit can induce substantial impacts on the optical, electrochemical, charge-transport properties and photovoltaic properties of the corresponding HTMs, but also demonstrate that the selenium-containing organic compounds are fascinating candidates for constructing dopant-free HTMs in PSC with both high efficiency and long stability being achieved.

Author contributions

Y.F. and Y.S. contributed equally to this work. Y.F. conceived the ideas and designed the research project. Y.S. fabricated and characterized devices. D.C. and H.Y. supervised and directed the research. Y.F. drafted and finalized this manuscript. All the authors revised this manuscript.

CRediT authorship contribution statement

Yajie Fu: Supervision, supervised and directed the research. **Huangzhong Yu:** Supervision, and. **Derong Cao:** Y.F. and Y.S. contributed equally to this work. Y.F. conceived the ideas and designed the research project. Y.S. fabricated and characterized devices.

Declaration of competing interest

The authors declare that they have no known competing financial interests or personal relationships that could have appeared to influence the work reported in this paper.

Acknowledgments

This work was supported by the National Natural Science Foundation of China (21772045, 22071066, 61974045), the Natural Science Foundation of Guangdong Province, China (2018B030311008, 2019A1515012092), and the Fund from the Guangzhou Science and Technology Project, China (201902010063).

Appendix A. Supplementary data

Supplementary data to this article can be found online at <https://doi.org/10.1016/j.dyepig.2021.109339>.

References

- Hodes G. Perovskite-based solar cells. *Science* 2013;342(6156):317–8.
- Brenner TM, Egger DA, Kronik L, Hodes G, Cahen D. Hybrid organic–inorganic perovskites: low-cost semiconductors with intriguing charge-transport properties. *Nat Rev Mater* 2016;1:15007.
- Zhang F, Shi W, Luo J, Pellet N, Yi C, Li X, et al. Isomer-pure bis-PCBM-assisted crystal engineering of perovskite solar cells showing excellent efficiency and stability. *Adv Mater* 2017;29(17):1606806.
- Zhang F, Bi D, Pellet N, Xiao C, Li Z, Berry JJ, et al. Suppressing defects through the synergistic effect of a Lewis base and a Lewis acid for highly efficient and stable perovskite solar cells. *Energy Environ Sci* 2018;11(12):3480–90.
- NREL best research-cell efficiency chart. <https://www.nrel.gov/pv/cell-efficiency.html>.
- Green MA, Ho-Baillie A, Snaith HJ. The emergence of perovskite solar cells. *Nat Photonics* 2014;8(7):506–14.
- Ye S, Rao H, Yan W, Li Y, Sun W, Peng H, et al. A strategy to simplify the preparation process of perovskite solar cells by Co-deposition of a hole-conductor and a perovskite layer. *Adv Mater* 2016;28(43):9648–54.
- Caló L, Kazim S, Grätzel M, Ahmad S. Hole-transport materials for perovskite solar cells. *Angew Chem Int Ed* 2016;55(47):14522–45.
- Fu Y, Li Y, Zeng Q, Wu H, Wang L, Tang H, et al. Influence of donor units on spiro [fluorene-9,9'-xanthene]-based dopant-free hole transporting materials for perovskite solar cells. *Sol Energy* 2021;216:180–7.
- Wang B, Zeng Q, Sun Z, Xue S, Liang M. Molecularly engineering of truxene-based dopant-free hole-transporting materials for efficient inverted planar perovskite solar cells. *Dyes Pigments* 2019;165:81–9.
- Zhang H, Wu Y, Zhang W, Li E, Shen C, Jiang H, et al. Low cost and stable quinoxaline-based hole-transporting materials with a D–A–D molecular configuration for efficient perovskite solar cells. *Chem Sci* 2018;9(27):5919–28.
- Hua Y, Zhang J, Xu B, Liu P, Cheng M, Kloo L, et al. Facile synthesis of fluorene-based hole transport materials for highly efficient perovskite solar cells and solid-state dye-sensitized solar cells. *Nano Energy* 2016;26:108–13.
- Kadro JM, Hagfeldt A. The end-of-life of perovskite PV. *Joule* 2017;1:29–46.
- Nguyen WH, Bailie CD, Unger EL, McGehee MD. Enhancing the hole-conductivity of spiro-OMeTAD without oxygen or lithium salts by using spiro(TFSD)2 in perovskite and dye-sensitized solar cells. *J Am Chem Soc* 2014;136(31):10996–1001.
- Carrillo J, Guerrero A, Rahimnejad S, Almora O, Zarazua I, Mas-marza E, et al. Ionic reactivity at contacts and aging of methylammonium lead triiodide perovskite solar cells. *Adv Energy Mater* 2016;6(9):1502246.
- Kasparavicius E, Magomedov A, Malinauskas T, Getautis V. Long-term stability of the oxidized hole transporting materials used in perovskite solar cells. *Chem Eur J* 2018;24(39):9910–8.
- Yang X, Wang H, Cai B, Yu Z, Sun L. Progress in hole-transporting materials for perovskite solar cells. *J Energy Chem* 2018;27(3):650–72.
- Pham HD, Jain SM, Li M, Manzhos S, Feron K, Pitchaimuthu S, et al. Dopant-free novel hole-transporting materials based on quinacridone dye for high-performance and humidity-stable mesoporous perovskite solar cells. *J Mater Chem A* 2019;7(10):5315–23.
- Rakstys K, Igci C, Nazeeruddin MK. Efficiency vs. stability: dopant-free hole transporting materials towards stabilized perovskite solar cells. *Chem Sci* 2019;10(28):6748–69.
- Pham HD, Xianqiang L, Li W, Manzhos S, Kyaw AKK, Sonar P. Organic interfacial materials for perovskite-based optoelectronic devices. *Energy Environ Sci* 2019;12(4):1177–209.
- Wang Y, Chen W, Wang L, Tu B, Chen T, Liu B, et al. Dopant-free small-molecule hole-transporting material for inverted perovskite solar cells with efficiency exceeding 21%. *Adv Mater* 2019;31(35):1902781.
- Zeng Q, Li Y, Tang H, Fu Y, Liao C, Wang L, et al. Dopant-free dithieno[3',2':3,4; 2'',3'':5,6]benzo[1,2-d]imidazole-based hole-transporting materials for efficient perovskite solar cells. *Dyes Pigments* 2021;188:109241.
- Niu T, Zhu W, Zhang Y, Xue Q, Jiao X, Wang Z, et al. D-A- π -A-D-type dopant-free hole transport material for low-cost, efficient, and stable perovskite solar cells. *Joule* 2021;5(1):249–69.
- Planells M, Nikolka M, Hurhangee M, Tuladhar PS, White AJP, Durrant JR, et al. The effect of thiadiazole out-backbone displacement in indacenodithiophene semiconductor polymers. *J Mater Chem C* 2014;2(41):8789–95.
- Huang J, Zhu Y, Chen J, Zhang L, Peng J, Cao Y. Dithienobenzothiadiazole-based conjugated polymer: processing solvent-relied interchain aggregation and device performances in field-effect transistors and polymer solar cells. *Macromol Rapid Commun* 2014;35(22):1960–7.
- Efrem A, Lim CJ, Lu Y, Ng SC. Synthesis and characterization of dithienobenzothiadiazole-based donor-acceptor conjugated polymers for organic solar cell applications. *Tetrahedron Lett* 2014;55(35):4849–52.
- Efrem A, Lei Y, Wu B, Wang M, Ng SC, Ong BS. Dithienobenzochalcogenodiazole-based electron donor-acceptor polymers for organic electronics. *Dyes Pigments* 2016;129:90–9.
- Shi S, Tang L, Guo H, Uddin MA, Wang H, Yang K, et al. Bichalcogenophene imide-based homopolymers: chalcogen-atom effects on the optoelectronic property and device performance in organic thin-film transistors. *Macromolecules* 2019;52(19):7301–12.
- Yao H, Ye L, Zhang H, Li S, Zhang S, Hou J, et al. Molecular design of benzodithiophene-based organic photovoltaic materials. *Chem Rev* 2016;116(12):7397–457.
- Petra A, Bendikov M, Chand S. Poly(3,4-ethylenedioxy-selenophene) and its derivatives: novel organic electronic materials. *Acc Chem Res* 2014;47(5):1465–74.
- Kawashima K, Osaka I, Takimiya K. Effect of chalcogen atom on the properties of naphthobis(chalcogenodiazole)-based π -conjugated polymers. *Chem Mater* 2015;27(19):6558–70.

- [32] García-Benito I, Zimmermann I, Urieta-Mora J, Aragón J, Calbo J, Perles J, et al. Heteroatom effect on star-shaped hole-transporting materials for perovskite solar cells. *Adv Funct Mater* 2018;28(31):1801734.
- [33] Oyama T, Yang YS, Matsuo K, Yasuda T. Effects of chalcogen atom substitution on the optoelectronic and charge-transport properties in picene-type π -systems. *Chem Commun* 2017;53(27):3814–7.
- [34] Gregory SA, Menon AK, Ye S, Seferos DS, Reynolds JR, Yee SK. Effect of heteroatom and doping on the thermoelectric properties of poly(3-alkylchalcogenophenes). *Adv Energy Mater* 2018;8(34):1802419.
- [35] Lee J, Sin DH, Clement JA, Kulshreshtha C, Kim HG, Song E, et al. Medium-bandgap conjugated polymers containing fused dithienobenzochalcogenadiazoles: chalcogen atom effects on organic photovoltaics. *Macromolecules* 2016;49(24):9358–70.
- [36] Arroyave FA, Richard CA, Reynolds JR. Efficient synthesis of benzo[1,2-b:6,5-b'] dithiophene-4,5-dione (BDTD) and its chemical transformations into precursors for π -conjugated materials. *Org Lett* 2012;14(24):6138–41.
- [37] Chen W, Liu T, Sun X, Guo F, Wang Y, Shi C, et al. Facile synthesis of simple arylamine-substituted naphthalene derivatives as hole-transporting materials for efficient and stable perovskite solar cells. *J Power Sources* 2019;425:87–93.
- [38] Zhang F, Wang S, Zhu H, Liu X, Liu H, Li X, et al. Impact of peripheral groups on phenothiazine-based hole-transporting materials for perovskite solar cells. *ACS Energy Lett* 2018;3(5):1145–52.
- [39] Ye X, Zhao X, Li Q, Ma Y, Song W, Quan Y-Y, et al. Effect of the acceptor and alkyl length in benzotriazole-based donor-acceptor-donor type hole transport materials on the photovoltaic performance of PSCs. *Dyes Pigments* 2019;164:407–16.
- [40] Zhang J, Xu B, Johansson MB, Vlachopoulos N, Boschloo G, Sun L, et al. Strategy to boost the efficiency of mixed-ion perovskite solar cells: changing geometry of the hole transporting material. *ACS Nano* 2016;10(7):6816–25.
- [41] Chamoulaud G, Bélanger D. Modification of ion-exchange membrane used for separation of protons and metallic cations and characterization of the membrane by current-voltage curves. *J Colloid Interface Sci* 2005;281(1):179–87.
- [42] Zhang X, Bi S, Zhou J, You S, Zhou H, Zhang Y, et al. Temperature-dependent charge transport in solution-processed perovskite solar cells with tunable trap concentration and charge recombination. *J Mater Chem C* 2017;5(36):9376–82.
- [43] Li Y, Xu Z, Zhao S, Qiao B, Huang D, Zhao L, et al. Highly efficient p-i-n perovskite solar cells utilizing novel low-temperature solution-processed hole transport materials with linear π -conjugated structure. *Small* 2016;12(35):4902–8.
- [44] Xie YM, Zeng Z, Xu X, Ma C, Ma Y, Li M, et al. FA-assisted iodide coordination in organic-inorganic wide-bandgap perovskite with mixed halides. *Small* 2020;16(10):1907226.